

Anomalous Structural Evolution and Glassy Lattice in Mixed-Halide Hybrid Perovskites

Shamim Shahrokhi, Milos Dubajic, Zhi-Zhan Dai, Saroj Bhattacharyya, Richard A. Mole, Kirrily C. Rule, Mohan Bhadbhade, Ruoming Tian, Nursultan Mussakhanuly, Xinwei Guan, Yuewei Yin, Michael P. Nielsen, Long Hu, Chun-Ho Lin, Shery L. Y. Chang, Danyang Wang, Irina V. Kabakova, Gavin Conibeer, Stephen Bremner, Xiao-Guang Li, Claudio Cazorla, and Tom Wu*

Hybrid halide perovskites have emerged as highly promising photovoltaic materials because of their exceptional optoelectronic properties, which are often optimized via compositional engineering like mixing halides. It is well established that hybrid perovskites undergo a series of structural phase transitions as temperature varies. In this work, the authors find that phase transitions are substantially suppressed in mixed-halide hybrid perovskite single crystals of $\text{MAPb}_{1-x}\text{Br}_x$ ($\text{MA} = \text{CH}_3\text{NH}_3^+$ and $x = 1$ or 2) using a complementary suite of diffraction and spectroscopic techniques. Furthermore, as a general behavior, multiple crystallographic phases coexist in mixed-halide perovskites over a wide temperature range, and a slightly distorted monoclinic phase, hitherto unreported for hybrid perovskites, is dominant at temperatures above 100 K. The anomalous structural evolution is correlated with the glassy behavior of organic cations and optical phonons in mixed-halide perovskites. This work demonstrates the complex interplay between composition engineering and lattice dynamics in hybrid perovskites, shedding new light on their unique properties.


1. Introduction

Recently, significant interest in hybrid organic-inorganic halide perovskites has arisen due to their extraordinary combination of optoelectronic properties such as optimal solar-matching bandgap, large absorption coefficient, high carrier mobility, long charge carrier lifetime, large diffusion length, and exceptional defect tolerance.^[1–5] As a class of emerging photovoltaic materials, three-dimensional hybrid halide perovskites have the general chemical formula ABX_3 consisting of a large organic cation A (e.g., $\text{MA} = \text{CH}_3\text{NH}_3^+$ or $\text{FA} = \text{CH}(\text{NH}_2)_2^+$), a metal cation B (e.g., Pb^{2+} or Sn^{2+}) and halide anions X (e.g., Cl^- , Br^- , or I^-). Precise control of the phases of hybrid perovskites is critical to their applications, and the phase

S. Shahrokhi, X. Guan, L. Hu, C.-H. Lin, S. L. Y. Chang, D. Wang, T. Wu
School of Materials Science and Engineering
Faculty of Science
University of New South Wales (UNSW)
Sydney, NSW 2052, Australia
E-mail: tom.wu@unsw.edu.au

M. Dubajic, N. Mussakhanuly, M. P. Nielsen, G. Conibeer, S. Bremner
School of Photovoltaic and Renewable Energy Engineering
University of New South Wales (UNSW)
Sydney, NSW 2052, Australia

Z.-Z. Dai, Y. Yin, X.-G. Li
Hefei National Laboratory for Physical Sciences at the Microscale
Department of Physics
University of Science and Technology of China (USTC)
Hefei 230026, China

 The ORCID identification number(s) for the author(s) of this article can be found under <https://doi.org/10.1002/smll.202200847>.

© 2022 The Authors. Small published by Wiley-VCH GmbH. This is an open access article under the terms of the Creative Commons Attribution License, which permits use, distribution and reproduction in any medium, provided the original work is properly cited.

DOI: 10.1002/smll.202200847

S. Bhattacharyya, M. Bhadbhade, R. Tian
Solid State and Elemental Analysis Unit
Mark Wainwright Analytical Centre
University of New South Wales (UNSW)
Sydney, NSW 2052, Australia

R. A. Mole, K. C. Rule
Australian Nuclear Science and Technology Organisation
Locked Bag 2001, Kirrawee DC NSW 2232, Australia

S. L. Y. Chang
Electron Microscope Unit
Mark Wainwright Analytical Centre
University of New South Wales (UNSW)
Sydney, NSW 2052, Australia

I. V. Kabakova
School of Mathematical and Physical Sciences
University of Technology Sydney
Sydney, NSW 2007, Australia

C. Cazorla
Departament de Física
Universitat Politècnica de Catalunya
Campus Nord B4-B5, Barcelona E-08034, Spain

transitions are known to be driven by thermodynamic variations such as temperature, electric field, and pressure, among which temperature is the most investigated.^[6–10] Deformation of metal-halide octahedra, which occurs due to a size mismatch between the A-site cation and metal-halide framework, can significantly affect the rotational movement of organic cations.^[11] For instance, MA reorientational motion is faster when smaller halide ions are incorporated at the X-site.^[12] Hybrid perovskites are generally in the cubic phase at high temperatures with the A-site cations rotating freely, while at low temperatures, they are in tetragonal and orthorhombic phases where the organic cation rotation is partially suppressed.^[13] The phase transitions in those materials are accompanied by the tilting of the BX_6 octahedra. In the tetragonal structures, in-phase octahedral tilting (e.g., all clockwise) along the z-direction denoted by $a^0a^0c^+$ leads to the $P4/mbm$ symmetry, while out-of-phase octahedral tilting denoted by $a^0a^0c^-$ leads to the $I4/mcm$ symmetry.^[14] Similarly, octahedral tilts of a^+b^- lead to the $Pnma$ symmetry in the orthorhombic structure.

Similar to many functional materials, the structural phases of hybrid perovskites are highly correlated with their physical properties. Particularly, the cubic and tetragonal phases are featured with a “crystalline liquid”-type behavior with the coexistence of coherent electronic transport and glassy phonon activities.^[15] A variety of experimental techniques have been used to detect structural phase transitions in hybrid perovskites. In a representative study, dielectric measurements revealed that $MAPbBr_3$ transforms from the cubic to the tetragonal structure at 236.3 K and then to an orthorhombic phase at 148.8 K.^[13] Moreover, an intermediate incommensurate phase was observed in $MAPbBr_3$ by single-crystal X-ray diffraction (SCXRD) and low-frequency Raman measurements.^[16] It is well established that the halide composition has a significant influence on the phase transitions in hybrid perovskites. The notable perovskite $MAPbI_3$ undergoes a transition from the cubic to the tetragonal phase near 330 K, and subsequently to an orthorhombic phase below 160 K.^[17–19] In general, these phase transitions are detected through discontinuities in the dielectric permittivity and heat capacity,^[13,20] solid-state nuclear magnetic resonance (NMR) line shapes,^[21] and/or splitting of X-ray diffraction peaks.^[18,22]

Although hybrid perovskites are very promising for optoelectronic applications, they suffer from instability issues caused by a variety of factors such as humidity, high temperature, intense light, and even interfacial reactions.^[23–24] It is well recognized that under ambient conditions, cubic-structured $MAPbBr_3$ is much more stable than tetragonal $MAPbI_3$,^[25] but the bandgap of $MAPbBr_3$ (2.27 eV) is too large for single-junction photovoltaic applications.^[26] To overcome the stability bottleneck, halide mixing has been developed as an effective compositional engineering strategy.^[27] In addition, mixed-halide perovskites have the benefit of bandgap tuning,^[23,28–29] which is indispensable for fabricating optoelectronic devices operating in the desired wavelength regimes. The phase transitions of hybrid perovskites are known to impact their photovoltaic applications,^[30] but there remain open questions regarding the temperature-dependent structures and phase transition mechanisms in mixed-halide hybrid perovskites.

In this work, we report the observation of the anomalous absence of abrupt phase transitions in mixed-halide hybrid

perovskites of $MAPbI_2Br_2$ and $MAPbI_2Br$, probed by a complementary suite of X-ray, dielectric, optical, and neutron spectroscopic techniques. A hitherto unreported monoclinic structure was found to coexist with the known cubic, tetragonal and orthorhombic structures in mixed-halide perovskites over a wide temperature range. Furthermore, first-principles calculations revealed the frustration of MA reorientational motion in the mixed-halide hybrid perovskites, thus corroborating the observation of the glassy behavior of organic cations. These findings may not only shed new light on the fundamental understanding of the physical properties of hybrid perovskites but also pave the way for realizing strategies to optimize the performance of perovskite devices.

2. Results and Discussion

Figure 1a illustrates the UV-Vis spectra of $CH_3NH_3PbI_{3-x}Br_x$ thin films. The onset of absorption shifts to higher wavelengths with increasing iodide quantity, i.e., from 542 nm for $MAPbBr_3$ to 600 nm for $MAPbI_2Br_2$, 700 nm for $MAPbI_2Br$, and 787 nm for $MAPbI_3$. Accordingly, the bandgaps extracted from the Tauc plots (**Figure 1b**) are 2.29, 2.11, 1.79, and 1.6 eV for $MAPbBr_3$, $MAPbI_2Br_2$, $MAPbI_2Br$, and $MAPbI_3$, respectively. Also, the pictures of as-grown single crystals indicate the change of the crystals to cubic shape with increasing bromide quantity, which is consistent with previously reported crystal shapes.^[31–32] In addition, normalized photoluminescence (PL) peak positions of related single crystals amount to 541, 578, 735, and 769 nm for $MAPbBr_3$, $MAPbI_2Br_2$, $MAPbI_2Br$, and $MAPbI_3$ (**Figure 1c**), respectively, and are consistent with previous reports, thus confirming the compositions of halide perovskites.^[33–34]

Differential scanning calorimetry (DSC) measurements were performed on the four single crystals to study the phase transition behavior. As shown in **Figure 1d**, the DSC curves of $MAPbI_3$ possess two reversible peaks with endothermic ones at 165 and 331 K in heating and exothermic ones at 329 and 158 K in cooling. Three reversible peaks were observed for $MAPbBr_3$ at 151, 156, and 236 K during heating and 234, 152, and 146 K during cooling (**Figure 1e**). The enthalpy and entropy changes of the corresponding peaks were derived from the area under the phase transition curves as $\Delta H = KA$ and $\Delta S = \Delta H/T_c$, in which K is the calorimetric constant of the instrument, A the peak area, and T_c the phase transition temperature (**Table S1**, Supporting Information).^[20] In general, the cubic-to-tetragonal transitions exhibit smaller energy and entropy changes than the tetragonal-to-orthorhombic ones.^[35] However, surprisingly, no thermal signals were observed in the DSC curves of mixed-halide perovskites (**Figure 1f**), which is in stark contrast with the sharp transitions recorded in the single-halide counterparts. The lack of DSC peaks suggests the absence of any abrupt heat exchange and phase transition in the mixed-halide perovskites.

Variable-temperature powder X-ray diffraction (VT-PXRD) measurements were performed to investigate the phase transitions in halide perovskites. For $MAPbI_3$, the split of the diffraction peaks of (200) at around $2\theta = 28^\circ$ and (210) at $2\theta = 32^\circ$ from room temperature down to 148 K is a signature of a tetragonal structure with a space group $I4/mcm$ (**Figure 2a**).^[22] Further cooling causes the emergence of an orthorhombic structure with space

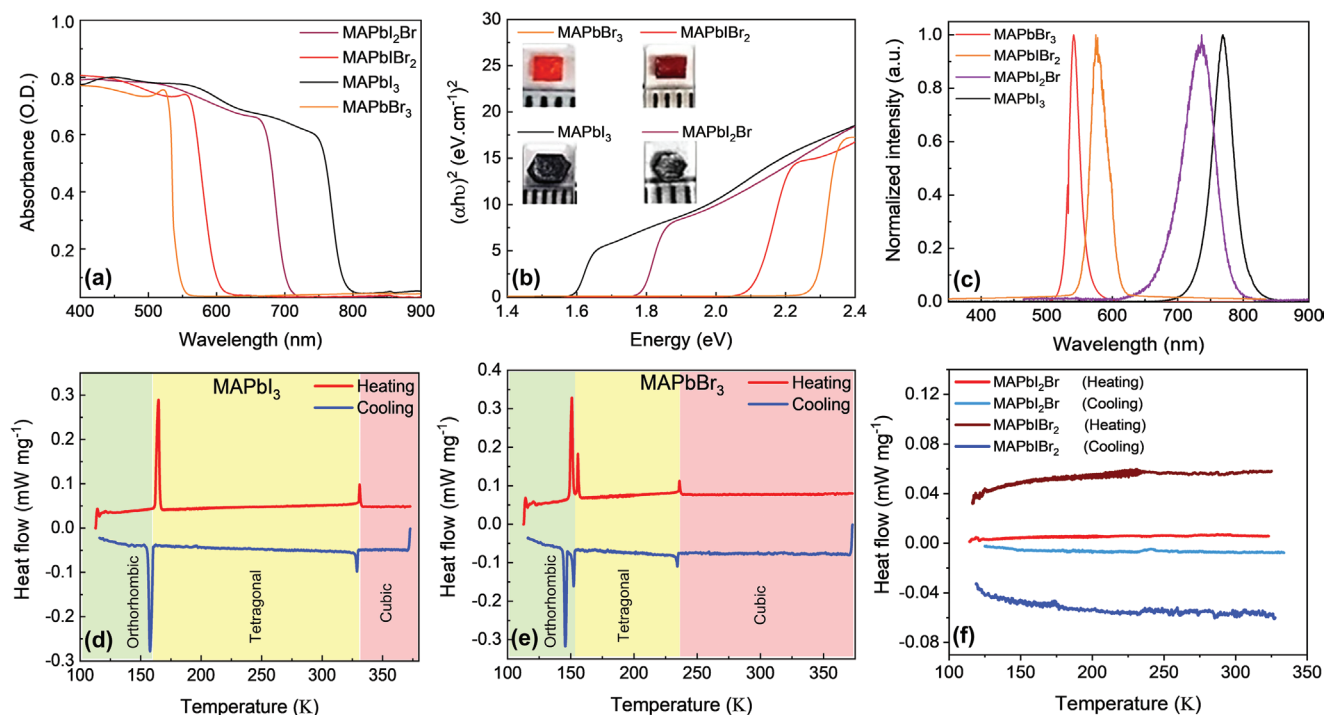


Figure 1. a) Absorption spectra of mixed-halide hybrid perovskites $\text{CH}_3\text{NH}_3\text{PbI}_{3-x}\text{Br}_x$. b) Tauc plots derived from a), and c) photoluminescence of $\text{CH}_3\text{NH}_3\text{PbI}_{3-x}\text{Br}_x$ single crystals with $x = 0, 1, 2$, and 3 . Insets: pictures of the corresponding grown crystals. Temperature dependence of DSC curves of d) MAPbI_3 , e) MAPbBr_3 , f) MAPbI_2Br , and MAPbIBr_2 single crystals measured during heating and cooling.

group $Pnma$. These structural changes are caused by rearrangements of the lead-halide octahedra, which progressively reduce the rotational motion of the MA cations.^[36] In MAPbBr_3 , there is no diffraction peak splitting at high temperatures, which is consistent with a cubic structure (space group $Pm-3m$) (Figure 2b). When the temperature decreases, phase transitions from cubic to tetragonal and then to orthorhombic structure are evidenced.

By contrast, the PXRD patterns of mixed-halide samples exhibit no apparent splitting in the diffraction peaks within the measured temperature range (Figure 2c,d), which leads to the conclusion that the lattices remain cubic or pseudo-cubic (i.e., structure close to cubic, but with some minor distortion). The diffraction patterns with labeled peaks at different temperatures are provided in Figure S1, Supporting Information. Meanwhile, broadening of the diffraction peaks was observed and intensified as the temperature decreased, which may indicate temperature-dependent lattice distortions including likely localized strains and multi-phase coexistence. Furthermore, single-crystal XRD experiments revealed the appearance of low-symmetry structures in mixed-halide samples at low temperatures (Figure S2, Supporting Information).

To account for such lattice distortions, in addition to cubic, tetragonal and orthorhombic structures were included in the PXRD fittings. The coexistence of tetragonal and orthorhombic structures across a certain temperature range has been previously reported in hybrid perovskites.^[37] This is further confirmed through simulated SCXRD patterns, which showed the existence of the orthorhombic structure in addition to the cubic phase (Figure S3, Supporting Information). As we will discuss in a later section, our first-principles calculations

predicted the existence of a monoclinic structure (space group Pm , Glazer's notation $a^0a^0a^0$) characterized by the absence of metal-halide octahedra tilts. Surprisingly, it was found that the addition of the monoclinic phase notably improves the PXRD fittings, as shown in Figure S4, Supporting Information. Such a monoclinic phase has been previously observed in ferroelectric oxide perovskites such as $\text{PbZr}_{0.52}\text{Ti}_{0.48}\text{O}_3$ (PZT) and BiFeO_3 (BFO),^[37–39] but to the best of our knowledge, it has not been reported for any mixed-halide hybrid perovskites.

The weight% of monoclinic, cubic, tetragonal, and orthorhombic phases in MAPbI_2Br obtained from PXRD fittings at different temperatures, are plotted in Figure 2e. The Rietveld refinement profiles are given in Figures S5 and S6, Supporting Information. The monoclinic structure appears to be the dominant one for the mixed-halide perovskites across almost the entire temperature range, while small percentages of cubic, tetragonal and orthorhombic phases were also present. The weight% of the monoclinic phase is 71% at room temperature and reduced as the temperature decreases. This result, along with the broadening of PXRD peaks, indicates a reduction in the overall symmetry. As shown in Figure 2f, the overall trend of temperature-dependent phase weight% in MAPbIBr_2 is similar to that in MAPbI_2Br , except that the monoclinic structure holds an even greater proportion (approximately 85% at room temperature), which is consistent with the expected smaller distortion caused by Br atoms compared to I atoms. Furthermore, the tetragonal and orthorhombic phases emerge in MAPbIBr_2 only below 228 and 220 K, respectively.

The temperature-dependent monoclinic angle and lattice parameters of both mixed-halide hybrid perovskites are shown

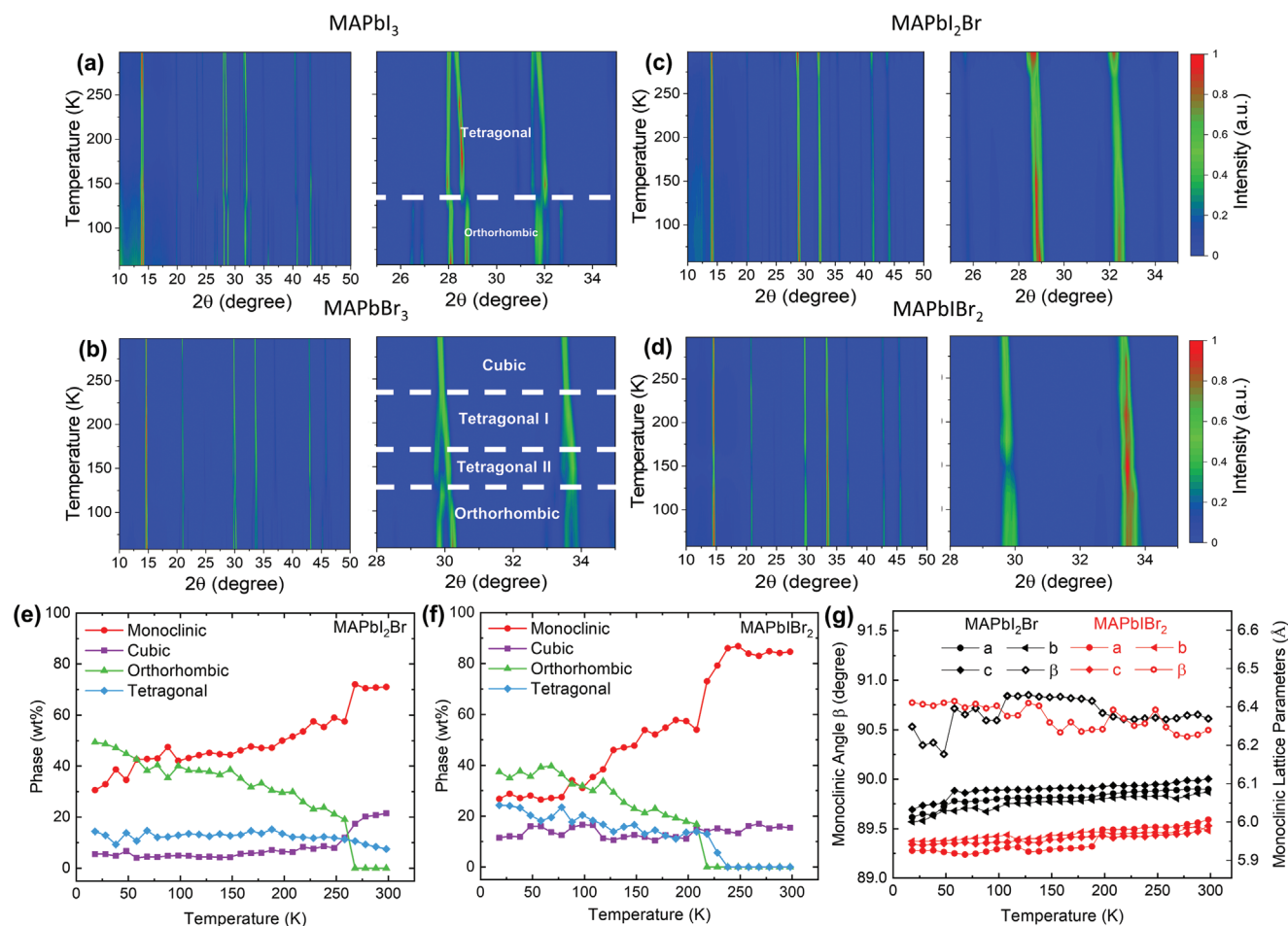


Figure 2. Variable-temperature powder X-ray diffraction (VT-PXRD) patterns of a) MAPbI₃, b) MAPbBr₃, c) MAPbI₂Br and d) MAPbIBr₂. The splittings of peaks at the phase transition temperatures are marked for MAPbI₃ and MAPbBr₃. Temperature-dependent phase weight% of e) MAPbI₂Br and f) MAPbIBr₂. Besides the cubic (space group: *Pm-3m*), orthorhombic (*Pnma*), and tetragonal (*I4/mcm*) phases previously reported for halide perovskites, a hitherto unreported monoclinic (*Pm*) phase with slight lattice distortion was discovered. g) Monoclinic angle β and pseudo-cubic lattice parameters of the mixed-halide hybrid perovskites.

in Figure 2g. It can be seen that the distortion angles are smaller than one degree with no discernible temperature-dependent trend beyond the experimental uncertainties. Besides, the monoclinic lattice parameters increase with temperature due to expansion of the unit cell, with MAPbI₂Br indicating higher values as compared to MAPbIBr₂. In order to justify the existence of the monoclinic structure in mixed-halide perovskites, the same Rietveld refinements were performed on single-halide hybrid perovskites, MAPbI₃ and MAPbBr₃. As shown in Figure S7, Supporting Information, it was found that the weight% of monoclinic structure is 0% and 0.1% in MAPbI₃ and MAPbBr₃, respectively, indicating that the single-halide perovskites do not exhibit any monoclinic-type distortion. In addition, the lattice parameters of different phases in mixed-halide perovskites decrease with decreasing temperature and are smaller than the lattice parameters of I-rich compounds (Figure S8, Supporting Information), which is consistent with the MAPbI₃ and MAPbBr₃ trends shown in Figure S9, Supporting Information. The schematic illustrations of MAPbI₂Br perovskite structures in monoclinic, tetragonal, and orthorhombic phases are presented in Figure S10, Supporting Information.

Temperature dependence of the real ϵ' and imaginary ϵ'' parts of the dielectric permittivity ($\epsilon^* = \epsilon' - i\epsilon''$) of the four perovskite single crystals were measured to shed light on the phase transitions. For MAPbI₃, the dielectric constant increases from 65.4 at room temperature to the maximum value of 99.8 at 165 K at a frequency of 1 MHz (Figure 3a), and this behavior can be attributed to the temperature-dependent rotational dynamics of MA dipoles.^[39] A sharp drop of the dielectric constant was observed at 155 K, which is caused by the first-order tetragonal-orthorhombic transition and the related (antipolar) ordering of the MA cations. The dielectric constant of MAPbBr₃ shows a similar trend except that there are two tetragonal structures between the cubic and orthorhombic ones.^[13,38]

In contrast, the temperature-dependent dielectric constants of MAPbI₂Br and MAPbIBr₂ single crystals follow a trend drastically different from the single-halide counterparts. As the most notable feature, there is no abrupt change during cooling in mixed-halide perovskites, and instead, broad peaks of ϵ' were observed (Figure 3a). In addition, the temperature-dependent dielectric loss is in line with the slower reorientation dynamics of the MA cations in mixed-halide hybrid

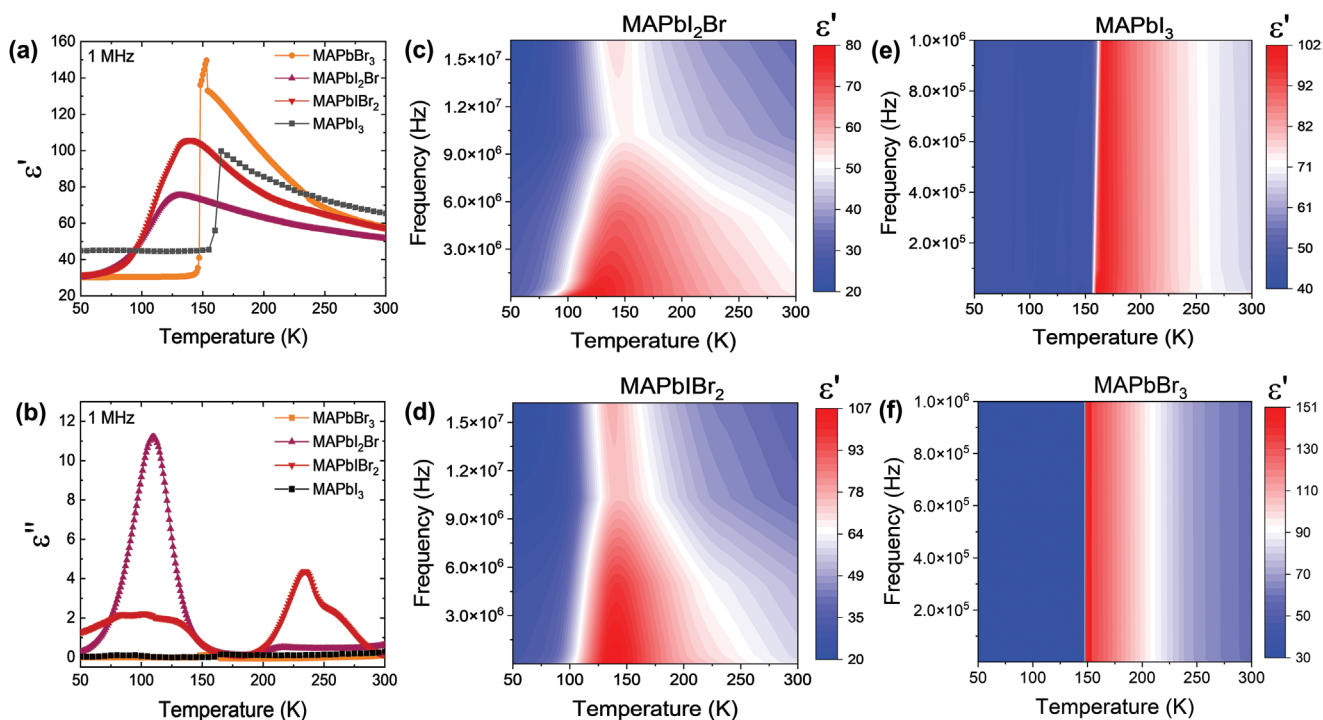


Figure 3. Temperature dependence of the a) real and b) imaginary parts of the dielectric permittivity of perovskite single crystals measured at 1 MHz. Temperature dependence of the real (ϵ') part of dielectric permittivity in c) MAPbI₂Br, d) MAPbI₂Br₂, e) MAPbI₃, and f) MAPbBr₃ single crystals measured at different frequencies during cooling.

single crystals^[40] (Figure 3b). The observed feature indicates the frustration of net electric dipoles, as recently reported in mixed-halide perovskites.^[41] Consistent with this scenario, a significant frequency dispersion was observed in the mixed-halide perovskites (Figure 3c,d): the ϵ' of MAPbI₂Br reaches the maximum at 97, 117, 131, and 143 K, at frequencies of 1 kHz, 100 kHz, 1 MHz, 15 MHz, respectively. For MAPbI₂Br₂, the dispersion is much less pronounced and the maxima of ϵ' occur at temperatures generally higher than those in the MAPbI₂Br counterpart. The high dielectric constants in these samples indicate ample rotational freedom of the MA cations^[42] and sizable ionic conductivity.^[40] In contrast, the dielectric constants of both MAPbI₃ and MAPbBr₃ single crystals show abrupt transitions and negligible frequency dispersion, indicating much less glassy characteristics (Figure 3e,f).

To assess the impact of halide mixing on the optical properties of MAPb(I_xBr_{1-x})₃, we performed variable-temperature PL measurements. Although surface properties are mostly characterized by PL measurement, some insights can be obtained on the phase transition behavior of the samples to support the PXRD data achieved from the bulk. To the best of our knowledge, the temperature-dependent PL behavior of mixed-halide perovskite MAPbI₂Br has not yet been reported. The color maps of normalized PL intensities as a function of temperature for MAPbI₃ and MAPbI₂Br single crystals are presented in Figure 4. In MAPbI₃, the PL peak exhibits a continuous blueshift as the temperature decreases to 148 K, followed by a redshift until 103 K and splitting of the PL peak at lower temperatures (Figure 4a). The unusual redshift of the PL peak is attributed to the stabilization of the valence band maximum.^[43]

These features are associated with the phase transition from tetragonal to orthorhombic structures,^[44] which is also captured by the anomalous variation in the full width at half maximum (FWHM) of the PL peak (Figure 4b). As the direct bandgap remains in the orthorhombic phase of MAPbI₃, the two PL peaks at temperatures between 100 and 110 K reflect the radiative recombination centers associated with intrinsic defects and residual tetragonal structures as well as the coexistence of both MA-ordered and MA-disordered orthorhombic domains.^[43,45–46]

In contrast, with decreasing temperature, MAPbI₂Br exhibited no abrupt change in PL peak position and FWHM (Figure 4c,d). The slight broadening of the PL emission peak with raising temperature can be attributed to the strong exciton-phonon interaction.^[47] Furthermore, the PL emission spectrum consists of a single peak without notable splitting, which indicates the dominance of the cubic and the slightly distorted monoclinic phases in the light-emitting property of mixed-halide perovskites. Another possible scenario is that the multiple co-existing phases as revealed by the XRD experiment possess very similar bandgaps, which leads to broad PL peaks without abrupt temperature-dependent transitions. The absence of abrupt phase transition was also observed in perovskites with a few other mixed-halide compositions including MAPbI_{3-x}Y_x (Y = Cl and Br) and (FAPbI₃)_{0.85}(MAPbBr₃)_{0.15}.^[47–48] This optical feature of mixed-halide perovskites is consistent with the suppression of phase transitions shown by the dielectric data enclosed in Figure 3.

Structural phase transitions can be directly observed by examining temperature-induced changes in elastic properties using Brillouin spectroscopy.^[49] Thus, to test our hypothesis

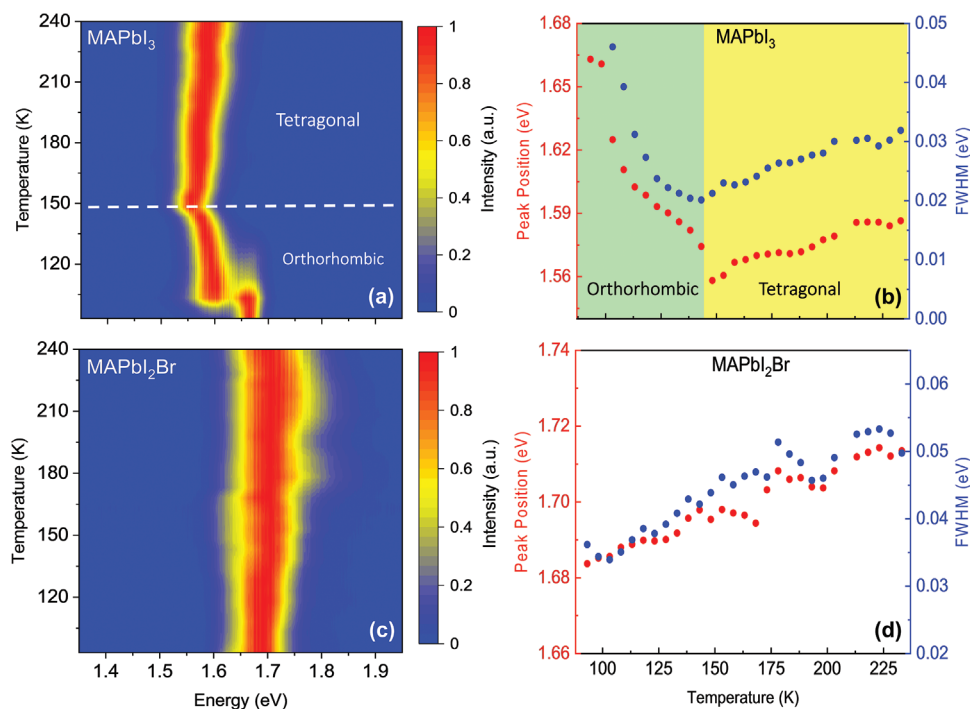


Figure 4. Color maps of normalized PL spectra of a) MAPbI₃ and c) MAPbI₂Br. PL peak position (red dots) and full width at half maximum (FWHM) (blue dots) of b) MAPbI₃ and d) MAPbI₂Br, respectively.

of suppressed phase transitions in mixed-halide hybrid perovskites, we collected Brillouin spectra in a broad temperature range (from 90 to 300 K) for two representative hybrid halide perovskites: one pure-halide MAPbBr₃ (Figure 5a) and the other mixed-halide MAPbIBr₂ (Figure 5c). The two distinct features in the Brillouin spectra, at 17 GHz–22 GHz and 6 GHz–8 GHz, are assigned to longitudinal (LA) and transverse acoustic (TA) phonons, respectively. By comparing Figure 5a,c, it is evident that both LA and TA phonons evolve similarly in the measured temperature range. LA and TA phonons first soften, i.e., decrease in frequency with decreasing temperature, down to 235 K in MAPbBr₃ and 220 K in MAPbIBr₂. The first temperature coincides with the cubic-tetragonal phase transition, which we observed with DSC (Figure 1e) and PXRD (Figure 2b) in MAPbBr₃. With the further temperature decrease, phonon frequencies increase, which is a signature of phonon hardening.

We will now focus on a narrow temperature range in the vicinity of the tetragonal-orthorhombic phase transition in MAPbBr₃ to further elucidate the differences in phase transitions between mixed- and single-halide perovskites. The representative Brillouin spectra are presented in Figures 5b,d, and details of data analysis can be found in the methods section. It is evident that the spectrum of MAPbBr₃ at $T = 138$ K differs significantly from the one at $T = 133$ K (Figure 5b). In MAPbIBr₂, however, all the spectra (Figure 5d) are similar across the measured temperature range. The stochastic reorientational dynamics of MA cations cause incoherent light scattering, which results in the observed quasielastic component (a tail of the broad Lorentzian at zero frequency) in the Brillouin spectra.^[50] The quasielastic component is present in the spectra of both crystals at higher temperatures. Upon the tetragonal-

orthorhombic phase transition in MAPbBr₃, MA cation reorientational dynamics are suppressed,^[51] which results in a complete disappearance of the quasielastic component at $T = 133$ K and $T = 123$ K (Figure 5b). However, in MAPbIBr₂, such a drastic change is not observed. Instead, the quasielastic component varied continuously with the decrease in temperature (Figure 5d). This behavior is comparable with a recent report that A-site and halide-site substituted perovskites exhibit suppressed phase transitions and altered reorientational dynamics of the A-site molecule.^[52] Thus, the difference in the low-temperature Brillouin spectra between MAPbBr₃ and MAPbIBr₂ indicates that the orthorhombic-tetragonal phase transition in mixed-halide hybrid perovskites is indeed suppressed.

In addition to the GHz range explored with the Brillouin spectroscopy, the composition-dependent structural phase transitions are accompanied by the significant changes in the THz phonon spectra.^[53] To explore the THz range that covers optical phonons, we employed inelastic neutron scattering (INS) spectroscopy to map the optical phonon density of states (pDOS). Optical phonons in the hybrid perovskites are known to show little dispersion and isotropic in reciprocal space.^[54–55] In Figure 6a–d, color maps of neutron scattering cross-section $S(\hbar\omega, Q)$ measured in the λ configuration ($\lambda = 4.69$ Å) for four samples at $T = 100$ K are presented. The figures reveal a stark difference between pure (MAPbBr₃ and MAPbI₃) and mixed halide (MAPbIBr₂ and MAPbI₂Br) samples. It is evident that the detected phonons are well defined for all wavevectors in the pure halide samples, whereas they are blurred out for the mixed-halide counterparts.

Figure 6e presents the integrated data from Figure 6a–d in the form of generalized phonon density of states (GDOS), which applies a slight modification on pDOS to account for

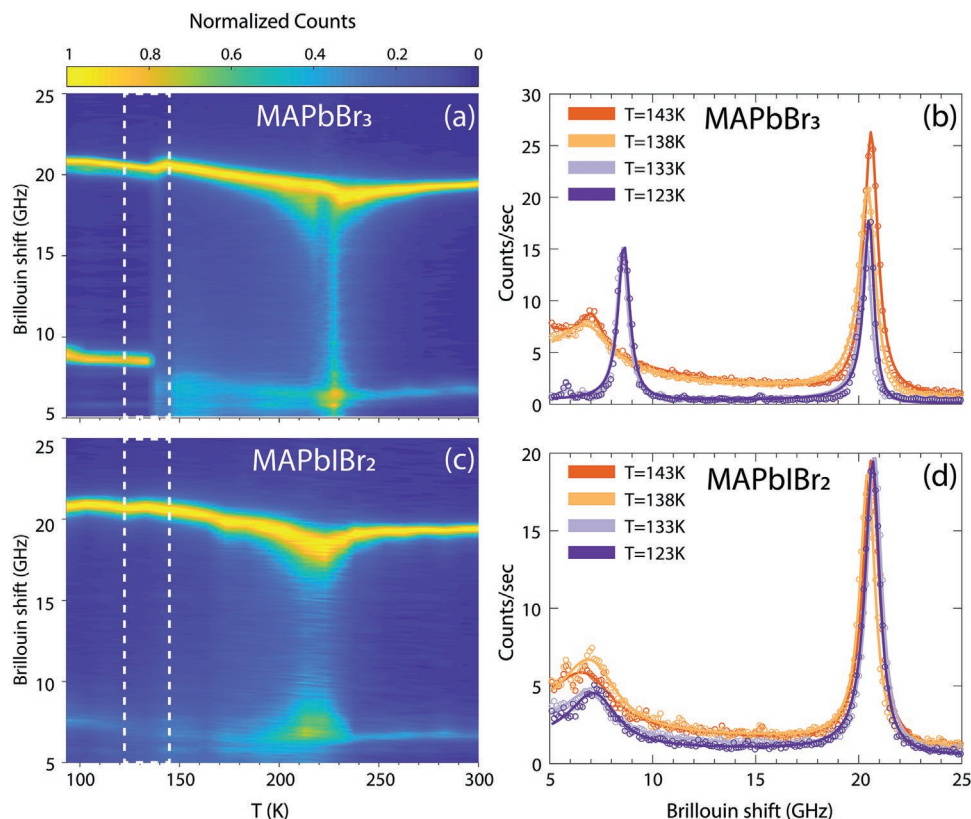


Figure 5. Normalized temperature-dependent color maps of Brillouin spectra measured in a) MAPbBr₃ and c) MAPbI₂Br₂. Brillouin spectra of b) MAPbBr₃ and d) MAPbI₂Br₂ measured at four different temperatures. Temperatures are selected to be in the vicinity of MAPbBr₃ orthorhombic to tetragonal phase transition. The selected spectra correspond to the vertical slices of the area framed with dashed rectangles in (a) and (c). The solid lines in (b) and (d) are fits to the experimental data.

the phonon thermal population factor (see the method section). The peaks correspond to optical phonon modes involving solely inorganic lattice (ω_1 , ω_2 , and ω_3) and inorganic-organic coupled modes (ω_{c1} , ω_{c2}). The detailed mode assignment is given in Table S2, Supporting Information. The integrated data, proportional to pDOS in the $\lambda/2$ configuration, are presented in Figure 6f. While the optical phonon mode (ω_1) at 2 meV is well defined in MAPbI₃ and broadened in MAPbBr₃, it is fully damped in MAPbI₂Br₂ and MAPbI₂Br. Furthermore, compared to the single-halide counterparts, the organic-inorganic lattice coupled mode (ω_{c1}) at 11 meV appears significantly more damped in the mixed-halide perovskites. The same dependence of the phonon modes on the halide composition was also observed at 1.5 K (Figure S11, Supporting Information).

The suppression of the phase transitions in the mixed-halide samples leads to less defined optical phonon modes, a signature of a glassy lattice. Upon the tetragonal-orthorhombic phase transition in pure-halide perovskites, MA molecules lose their stochastic character and take a more preferential direction in the unit cells. If there is a regular arrangement of neighboring MA molecules with long-range order, it would lead to sharp optical phonons due to increased crystallinity of the organic sublattice (Figure S12, Supporting Information). That is the case in MAPbI₃, where MA molecules are antiferroelectrically ordered in the orthorhombic phase.^[56] However, in mixed-halide perovskites, abrupt phase transition does not occur. Upon lowering

the temperature, MA molecular motions slow down until they are quenched. Therefore, static MA cations are randomly oriented and no long-range order is established. In other words, the organic sublattice formed by MA molecules is glassy (amorphous), while the inorganic lattice remains crystalline. This coexistence of crystalline and glassy lattices results in less defined optical phonons, as observed in mixed-halide hybrid perovskites.

In order to better understand the possible mechanisms leading to the absence of phase transitions and the MA reorientational motion in mixed-halide hybrid perovskites, we performed extensive first-principles calculations based on density functional theory (DFT, Experimental Section). In particular, we calculated 1) the mixing enthalpy of MAPbI₂Br and MAPbI₂Br₂ in their pseudo-cubic, tetragonal and orthorhombic phases and 2) the MA rotation autocorrelation function of cubic MAPbI₃, MAPbBr₃, MAPbI₂Br and MAPbI₂Br₂ at different temperatures.

After the DFT geometry relaxations, we found that the cubic phase of MAPbI₂Br and MAPbI₂Br₂ underwent small monoclinic distortions of 1.66 and 0.32°, respectively (Figure 7a,b), which is in line with the XRD result. For all mixed-halide phases, the lowest energies were obtained for configurations in which the less abundant halide ions (e.g., I for MAPbI₂Br₂) were surrounded by eight of the more abundant halide ions (e.g., Br for MAPbI₂Br₂). Analogous to the pure MAPbI₃ and MAPbBr₃ cases, we found that monoclinic mixed-halide perovskites have higher DFT energies than the corresponding tetragonal and

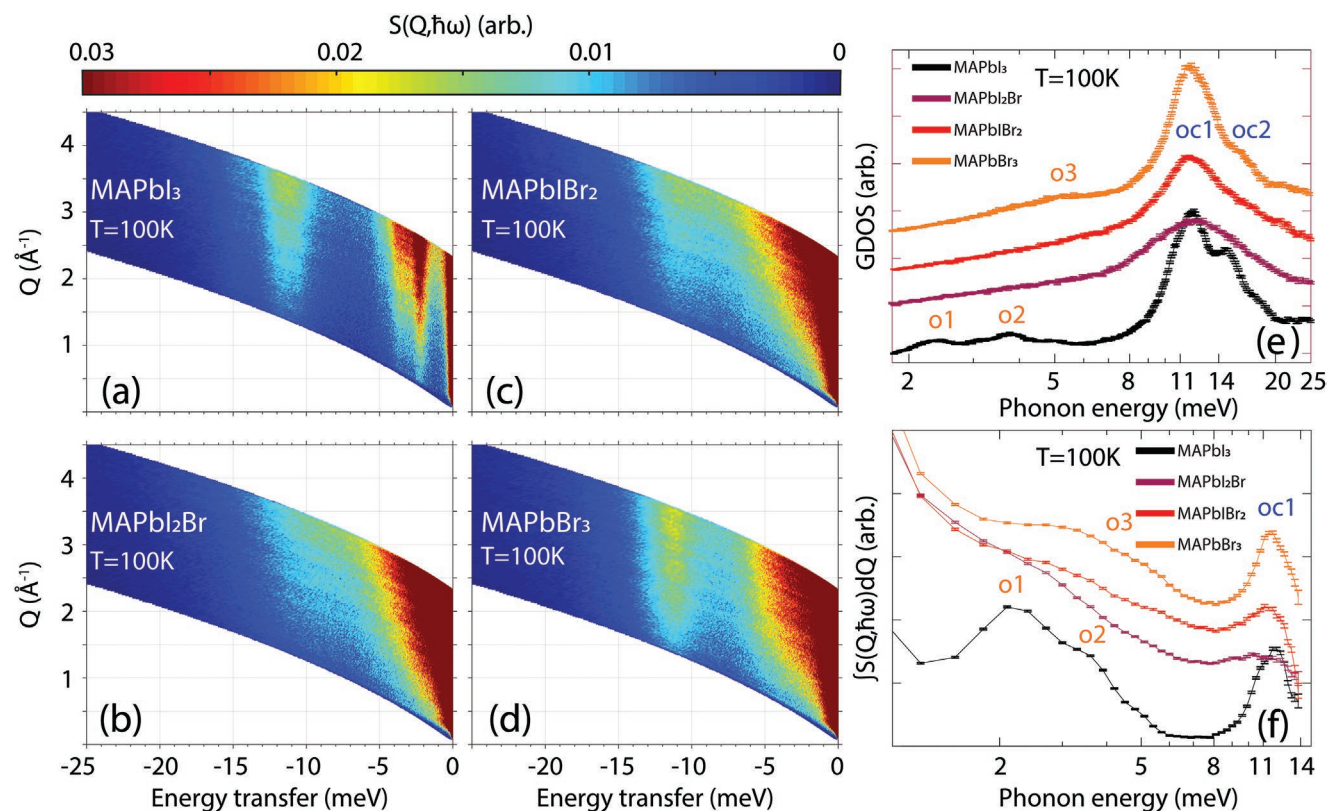


Figure 6. Neutron scattering cross-section $S(Q, \hbar\omega)$ at $T = 100$ K of a) MAPbI_3 , b) MAPbI_2Br , c) MAPbIBr_2 , and d) MAPbBr_3 , measured in the λ configuration; Q corresponds to phonon wavevector and $\hbar\omega$ to phonon energy. e) Generalized phonon density of states (GDOS) extracted from the data in (a–d). f) Plot of $\int S(Q, \hbar\omega) dQ$ (proportional to phonon density of states) as a function of phonon energy, measured in $\lambda/2$ configuration. Optical inorganic (o1, o2, and o3) and optical organic-inorganic (oc1, oc2) phonon modes are labeled.

orthorhombic phases (e.g., $E_C - E_T = 61$ and 13 meV per formula unit (f.u.) for MAPbI_2Br and MAPbIBr_2 , respectively). This computational result appears to be in contradiction with the experimental observation that the monoclinic structures of mixed-halide perovskites persist down to low temperatures.

Interestingly, however, our DFT calculations of the mixing enthalpy, H_{mix} for the three phases of MAPbI_2Br and MAPbIBr_2 (Experimental Section) show that at low temperatures only the slightly distorted phase is stable against decomposition into the end-members MAPbI_3 and MAPbBr_3 (Figure 7c). For instance, MAPbIBr_2 presents the lowest H_{mix} value of -37 meV per f.u. for the monoclinic phase and the highest H_{mix} value of $+40$ meV per f.u. for the orthorhombic phase. Therefore, we may conclude that as the temperature drops mixed-halide perovskites tend to remain dynamically arrested in the cubic and slightly distorted monoclinic phases due to the impassable energy barriers accompanying the chemical decomposition of the energetically more favorable tetragonal and orthorhombic phases.

In our ab initio molecular dynamics simulations, we found that at $T = 250$ K and 400 K both cubic MAPbI_3 and MAPbBr_3 present very high MA reorientational motion characterized by similar MA reorientational frequencies and correlation times (Figure 7d). More importantly, in good agreement with our experimental observations, MA reorientational motion turns out to be significantly hindered in mixed-halide perovskites, as evidenced by the time decay estimated for the MA rotation

autocorrelation function. The main reason for the blockage of MA rotation in mixed-halide perovskites is the disruption of the highly symmetric and shallow potential environment experienced by the molecular anions in cubic MAPbI_3 and MAPbBr_3 .

The appearance of a monoclinic distortion in the cubic phase and the chemical disorder in the MA halide coordination (Figure 7a,b) establish a preferential direction for MA orientation and thus are ultimately responsible for the partial frustration of MA reorientational motion. As the systems are quenched from high to low temperature, the lack of abrupt phase transformations and the freezing of MA rotations naturally lead to the appearance of an orientational glass phase. Furthermore, the theoretical vibrational density of states was calculated for MAPbIBr_2 and MAPbI_2Br at 250 K (Figure S13, Supporting Information). The results were in reasonable agreement with the experimental pDOS (Figure 6f), featuring broad energy peaks at 11 meV and significantly damped modes at lower energies.

3. Conclusion

In this work, a suite of complementary techniques has been applied to shed light on the lattice structures and cation dynamics in mixed-halide hybrid perovskites. The materials remain mainly in the pseudo-cubic phases, i.e., the combination of cubic and slightly monoclinic, with small percentages

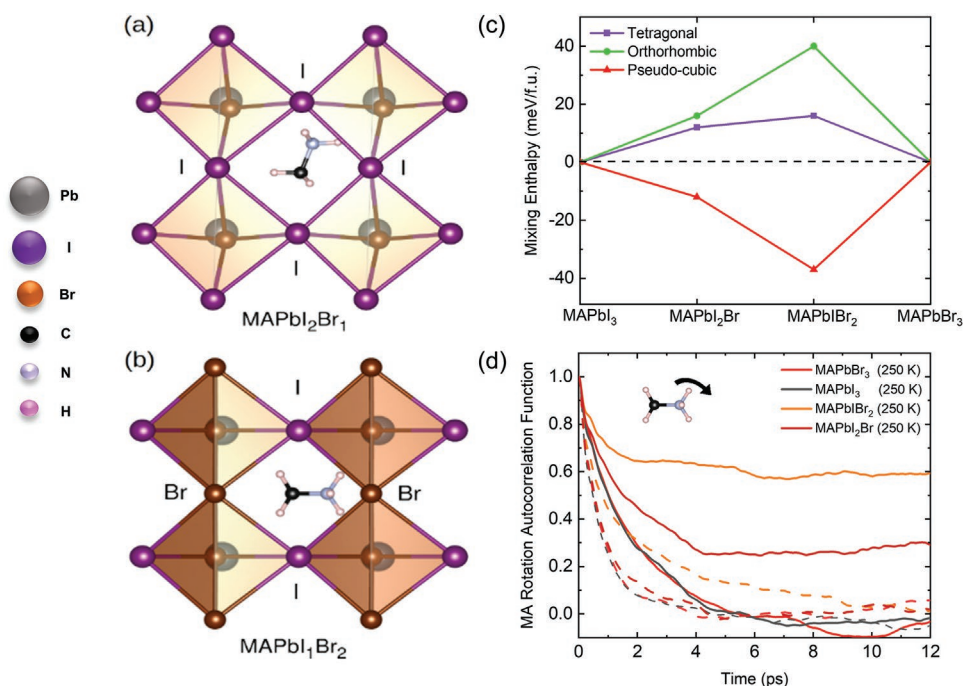


Figure 7. Detail of the optimum arrangement of halide ions around the MA cations obtained for a) MAPbI_2Br and b) $\text{MAPbI}_1\text{Br}_2$ (some atoms have been removed for clarity). c) Density functional theory (DFT) mixing enthalpy obtained for the tetragonal, orthorhombic, and pseudo-cubic phases of mixed-halide hybrid perovskites; positive (negative) H_{mix} values indicate a tendency for the system to (not) decompose into the endmembers MAPbI_3 and MAPbBr_3 . d) MA rotation autocorrelation function results obtained from ab initio molecular dynamics simulations for pure and mixed halide hybrid perovskites at 250 K; rapidly (slowly) decaying autocorrelation functions indicate high (low) frequency MA reorientational motion. Dashed lines represent results obtained at a high temperature of 400 K.

of tetragonal and orthorhombic phases. Compared to the pure halide counterparts, a much glassier lattice of mixed-halide perovskites was revealed, indicating the frustration of MA reorientational motions as well as slower molecular dynamics. Moreover, halide mixing seems to promote the crystal-liquid duality in hybrid perovskites over a much wider temperature range compared to the single-halide counterparts. These observed characteristics of mixed-halide perovskites are ultimately responsible for the suppression of phase transitions and the coexistence of several structures. The discovered dominance of high-symmetry structures in mixed-halide perovskites and their persistence in a wide range of temperatures have significant implications for optoelectronic applications, particularly on the enhanced ambient stability compared to the pure-halide endmembers. The anomalous suppression of long-range structural order contributes to the unique electronic and phonon characteristics of hybrid perovskites with engineered mixed-cation and/or mixed-halide compositions. An in-depth understanding of the dynamics of orientational MA cations and the glassy behavior of the perovskite lattice provide new clues for improving the performance and stability of perovskite-based devices.

4. Experimental Section

Chemicals and Reagents: Lead bromide ($\geq 98\%$) and lead iodide (99.999% trace metals basis) were purchased from Sigma Aldrich. MABr and MAI were purchased from Dyesol (Australia). N,N-dimethylformamide (DMF) (99.8%) and g-butyrolactone (GBL)

($>98\%$) solvents were purchased from RCI Labscan and TCI (Tokyo Chemical Industry), respectively. All salts and solvents were used as received without any further purification.

Sample Preparation: Inverse temperature crystallization method was used in synthesizing the single crystals. A mixture of MAX and PbX_2 ($X = \text{I}$ or Br) was dissolved in GBL and DMF solvents to prepare 0.8 and 1 molar solutions of MAPbI_3 and MAPbBr_3 , respectively. For MAPbI_2Br and $\text{MAPbI}_1\text{Br}_2$, 0.9 molar solutions were synthesized in mixed solvents of GBL and DMF (2:1 and 1:2 ratios, respectively). The bromide solution was prepared at room temperature, whereas the others were heated up to 60°C until the powders were dissolved thoroughly. Then, the solutions were filtered by PTFE filters with $0.45\ \mu\text{m}$ pore size, and 3 ml of the filtrates were placed in a beaker on a hot plate. The temperatures of the solutions were gradually increased to 120°C for mixed-halide perovskite solutions and 100 and 150°C for MAPbBr_3 and MAPbI_3 , respectively. The crystals were grown for 3 h under ambient conditions. For the optical absorption measurements, thin films were prepared from precursors, which were fabricated by dissolving a mixture of MAX and PbX_2 ($X = \text{I}$ or Br) in 1 ml of DMF and DMSO solvents (DMF:DMSO = 4:1 for mixed-halide perovskites). The perovskite precursor solution was spin-coated onto the substrate at 1000 rpm for 10 s and 4000 rpm for 30 s using anti-solvent chlorobenzene, followed by heating at 100°C for 10 min.

DSC and XRD Measurements: DSC measurements were performed on a Netzsch DSC. Proteus 204 F1 in aluminum crucible under nitrogen atmosphere. The single crystals were cooled and heated in the temperature range of 115 – $330\ \text{K}$ with a scan rate of $10\ \text{K}\ \text{min}^{-1}$. Variable-temperature X-ray Diffraction measurements were conducted on a PANalytical Empyrean system fitted with a copper tube ($\lambda = 1.5406\ \text{\AA}$) and a PIXcel detector. The sample stage was configured with Oxford Phenix cryostat to perform data collection at low temperatures. The sample height alignment was performed so that the data collection error could be minimized. Data collection was performed over a 2θ range of 10 – 95° with a step size of 0.026° and a measurement time of 550 s

per step. Raw data were collected from ambient temperature to 18 K. The raw data were processed using HighScore Plus software (Supplier: PANalytical BV, The Netherlands). A full pattern Rietveld fit was performed on the raw PXRD data with the crystallographic information files (cif) derived from the SCXRD data and DFT calculations. More details on data analysis are provided in Supporting Information.

Dielectric Measurement: For dielectric measurements, opposite faces of the perovskite single crystals were painted with silver paste as electrodes, and the samples were positioned inside the cryostat of a physical property measurement system (Quantum Design, PPMS-9T), with the temperature controlled in the range from 50 to 300 K. Dielectric constants and dissipation factors at various temperatures were measured using a LCR meter (Agilent 4294A) with an AC voltage of 0.5 V.

Brillouin Microspectroscopy Measurements: Brillouin microspectroscopy measurements reveal low-frequency (GHz) acoustic phonon spectra of perovskite single crystals. These measurements were carried out using a single-frequency continuous-wave laser ($\lambda = 660$ nm, 200 mW, Torus Laser Quantum) and a scanning, 6 pass tandem Fabry–Pérot interferometer (TFPI, JRS Instruments). The samples were positioned inside the FTIR600 cryostat stage (Linkam Scientific), with temperature controlled externally in the range from 100 to 300 K. The direction of the probing laser beam was chosen collinear with the axis of symmetry (100) for crystalline cubic phase while the scattered light was collected in backscattering geometry. The average acquisition time per measurement was chosen between 30 and 300 s depending on the signal strength, but overall giving rise to a signal-to-noise ratio of at least 10^3 . The long-distance objective lens used for this measurement had a numerical aperture of $NA = 0.42$ and resulted in an approximate focal volume of $2 \mu\text{m} \times 2 \mu\text{m} \times 50 \mu\text{m}$ for X, Y, and Z directions, respectively. Two phonon modes were detected at each spatial location and temperature setting: 1) high-frequency longitudinal acoustic (LA) mode and 2) low-frequency quasi-transverse mode (TA). The data for the low-energy TA mode was fitted using the Lorentzian profile convoluted with the instrument response function (measured at each temperature). The high-energy LA mode experimental data was successfully described with the model,^[50] which assumes coupling between LA and quasielastic peak at zero frequency originating from the rotational MA modes.

PL Spectroscopy and Absorption Measurements: PL measurements were carried out in a custom build PL setup consisting of a continuous wave Thorlabs laser diode excitation source ($\lambda = 407$ nm), which was focused with a long-distance 15X metal (silver) objective lens (to minimize chromatic aberration induced distortion of collected PL spectra) of $NA = 0.3$ forming a $1.5 \text{ m} \times 1 \text{ e}^{-2}$ diameter spot on a sample's surface. The sample was mounted inside FTIR6000 (Linkam Scientific) liquid nitrogen cryostage. The PL was collected with the same objective, filtered with a 450 nm long-pass filter, and coupled to an optical fiber connected with a modular UV-VIS spectrometer (Ocean Insight). Spectra were acquired in temperature steps of 5 K, with a heating rate of 10 K min^{-1} and a waiting time of 1 min for the thermal equilibration between stage and a sample volume. Recorded spectra were fitted with Gaussian profiles and the corresponding peak position and FWHM parameters for each temperature were extracted to form Figure 5b,d. PerkinElmer LAMBDA1050 UV/Vis/NIR spectrophotometer with an integrating sphere module was used to measure transmittance (T) and reflectance (R) spectra of the thin film samples. Absorbance (A) was then calculated as $A = 1 - R - T$.

Neutron Scattering Measurement: INS experiments were performed on the time-of-flight cold-neutron spectrometer-Pelican,^[57–58] at the Australian Nuclear Science and Technology Organisation (ANSTO), Australia. Approximately 4g of powder samples were mounted in an annular aluminum sample can with a 0.5 mm gap. The sample was mounted in a sample stick CCR type cryostat with secondary He recirculation loop capable of measuring in the temperature range 1.5 to 800 K. The instrument was aligned for $\lambda = 4.69 \text{ \AA}$ (3.7 meV) incident neutrons and for $\lambda/2 = 2.35 \text{ \AA}$ (14.8 meV) neutrons which lead to the instrument resolution of 135 μeV and 0.7 meV, respectively. The intensity of an empty can was subtracted as the background contribution and the data were normalized to a vanadium standard that had the same geometry as the sample can. All data manipulations were performed

using the Large Array Manipulation Program (LAMP). The scattering function $S(Q, \hbar\omega)$, as a function of scattering wave vectors (Q) and phonon energy ($\hbar\omega$), were measured in both λ and $\lambda/2$ configuration on energy loss and gain mode, respectively, over a wide temperature range and then transformed to a GDOS using the following formula,

$$g(E) = \int \frac{\hbar\omega}{Q^2} S(Q, \hbar\omega) \left(1 - e^{-\frac{\hbar\omega}{k_B T}} \right) dQ \quad (1)$$

where k_B is Boltzmann's constant and T is temperature.

First-Principles Calculations: DFT calculations based on the PBEsol functional^[59] were performed with the VASP software.^[60] Wave functions were represented in a plane-wave basis set truncated at 750 eV, and a Monkhorst-Pack k -point grid of $12 \times 12 \times 12$ was used for reciprocal-space integrations within the first Brillouin zone (IBZ) of a 12-atoms unit cell. The “projected augmented wave” method was used to represent the ionic cores considering the following electronic states as valence: C 2s2p, H 1s, N 2s2p, Pb 6s6p, I 5s5p, and Br 4s4p. Geometry relaxations were performed for optimizing the structure of bulk MAPbI₃, MAPbBr₃, MAPbI₂Br, and MAPbIBr₂ in the corresponding cubic, tetragonal and orthorhombic phases at zero temperature, by using a conjugate-gradient algorithm that optimized the volume and shape of the unit cell as well as the atomic positions. The geometry relaxations were halted once the forces in all the atoms were smaller than 0.01 eV \AA^{-1} . Chemical disorder in the mixed-halide hybrid perovskites was simulated by generating all possible I/Br ionic arrangements compatible with a $1 \times 3 \times 3$ supercell containing nine formula units. Mixing enthalpies, H_{mix} , were calculated by considering ground-state energies and the formula:

$$H_{\text{mix}}(x) = H(\text{MAPbI}_{3x}\text{Br}_{3-3x}) - xH(\text{MAPbI}_3) - (1-x)H(\text{MAPbBr}_3) \quad (2)$$

where x represents the percentage of MAPbI₃ in the mixed compound. Positive H_{mix} values indicate that the crystal is thermodynamically prone to decompose into the end-members MAPbI₃ and MAPbBr₃ at low temperatures (i.e., when configurational entropy effects are negligible).

First-principles molecular dynamics (AIMD) simulations based on DFT^[61] were performed in the canonical (N, V, T) ensemble for cubic MAPbI₃, MAPbBr₃, MAPbI₂Br, and MAPbIBr₂. The selected unit cell volumes, geometries, and I/Br ionic arrangements were the same as determined at zero-temperature conditions (i.e., ground-state configurations). The temperature in the AIMD simulations was kept fluctuating around a set-point value by using Nose–Hoover thermostats. Large simulation boxes containing 324 atoms (that is, 27 formula units) were employed in all the AIMD simulations and periodic boundary conditions were applied along with the three corresponding pseudo-Cartesian directions. Newton's equation of motion was integrated by using the customary Verlet's algorithm and a time-step length of $\Delta t = 10^{-3}$ ps. Γ -point IBZ sampling was employed for all the AIMD simulations. The calculations comprised total simulation times of ≈ 100 ps and we performed two AIMD simulations per compound at $T = 400$ and 250 K. The rotation autocorrelation function of the molecular anions (MA) was estimated with the formula:

$$\Phi_{\text{MA}}(\tau) = \langle \mathbf{r}(t) \cdot \mathbf{r}(t + \tau) \rangle \quad (3)$$

where \mathbf{r} is a unitary vector connecting the C and N atoms in each MA and $\langle \dots \rangle$ denotes the thermal average for all MA over the total duration of the simulation.^[61] This autocorrelation function typically decays as $\exp[-\lambda_{\text{MA}} \tau]$, where the parameter λ_{MA} is positively defined and represents a characteristic reorientational frequency. When the MA reorientational motion is significant, that is, λ_{MA} is large, the Φ_{MA} function rapidly decreases to zero with time.

Supporting Information

Supporting Information is available from the Wiley Online Library or from the author.

Acknowledgements

C.C. acknowledged support from the Spanish Ministry of Science, Innovation, and Universities under the “Ramón y Cajal” fellowship RYC2018-024947-I. Computational resources and technical assistance were provided by the Australian Government and the Government of Western Australia through Magnus under the National Computational Merit Allocation Scheme and Pawsey Supercomputing Centre. The work at USTC was supported by NSFC (51790491). M.P.N. acknowledges support from the UNSW Scientia Program. I.V.K. acknowledges support from Australian Research Council through Discovery Program (DP190101973). M. D. acknowledges support by AINSE Limited through a PGRA award. All authors acknowledge beam time awarded by ANSTO through the proposal no. P8942 and thank Qiyuan Wu for his help with sample handling during neutron scattering experiments.

Open access publishing facilitated by University of New South Wales, as part of the Wiley - University of New South Wales agreement via the Council of Australian University Librarians.

Conflict of Interest

The authors declare no conflict of interest.

Author Contributions

S.S. and M.D. contributed equally to this work. T.W. conceived the idea, supervised the project, and revised the manuscript. S.S. and M.D. prepared the manuscript. S.S. provided single crystal and powder samples. N.M. prepared thin films. S.S. and M.D. performed optical measurements and analyzed the data. S.S. performed DSC measurements and analyzed the data. S.S. and S.B. performed PXRD measurements and analyzed the data. S.B. performed PXRD refinements and contributed to the data analysis. Z.D., Y.Y., and X.L. performed dielectric measurements and S.S. analyzed the data. M.D. and M.P.N. performed photoluminescence measurements and analyzed the data. M.D. and I.V.K. performed Brillouin scattering experiment and analyzed the data. R.A.M., M.D., K.C.R., G.C., and S.B. contributed to the INS measurements and data analysis. C.C. performed the DFT simulations and analyzed the data. M.B. and R.T. performed SCXRD measurements and contributed to the data analysis. S.L.Y.C. performed SCXRD simulations and analyzed the data. All authors participated in revising the manuscript.

Data Availability Statement

The data that support the findings of this study are available from the corresponding author upon reasonable request.

Keywords

glassy lattices, hybrid perovskites, mixed-halide, monoclinic, phase transitions

Received: February 9, 2022

Revised: April 9, 2022

Published online: April 28, 2022

- [1] V. Adinolfi, W. Peng, G. Walters, O. M. Bakr, E. H. Sargent, *Adv. Mater.* **2018**, *30*, 1700764.
 [2] D. W. deQuilettes, K. Frohna, D. Emin, T. Kirchartz, V. Bulovic, D. S. Ginger, S. D. Stranks, *Chem. Rev.* **2019**, *119*, 11007.
 [3] Y. Fu, H. Zhu, J. Chen, M. P. Hautzinger, X. Y. Zhu, S. Jin, *Nat. Rev. Mater.* **2019**, *4*, 169.

- [4] L. Gu, S. Poddar, Y. Lin, Z. Long, D. Zhang, Q. Zhang, L. Shu, X. Qiu, M. Kam, A. Javey, Z. Fan, *Nature* **2020**, *581*, 278.
 [5] A. Younis, C.-H. Lin, X. Guan, S. Shahrokhi, C.-Y. Huang, Y. Wang, T. He, S. Singh, L. Hu, J. R. D. Retamal, J.-H. He, T. Wu, *Adv. Mater.* **2021**, *33*, 2005000.
 [6] C. C. Stoumpos, C. D. Malliakas, M. G. Kanatzidis, *Inorg. Chem.* **2013**, *52*, 9019.
 [7] R. L. Milot, G. E. Eperon, H. J. Snaith, M. B. Johnston, L. M. Herz, *Adv. Funct. Mater.* **2015**, *25*, 6218.
 [8] B. Saparov, D. B. Mitzi, *Chem. Rev.* **2016**, *116*, 4558.
 [9] K. P. Goetz, A. D. Taylor, F. Paulus, Y. Vaynzof, *Adv. Funct. Mater.* **2020**, *30*, 1910004.
 [10] J.-H. Lee, A. Jaffe, Y. Lin, H. I. Karunadasa, J. B. Neaton, *ACS Energy Lett.* **2020**, *5*, 2174.
 [11] S. Maheshwari, M. B. Fridriksson, S. Seal, J. Meyer, F. C. Grozema, *J. Phys. Chem. C* **2019**, *123*, 14652.
 [12] O. Selig, A. Sadhanala, C. Müller, R. Lovrincic, Z. Chen, Y. L. A. Rezus, J. M. Frost, T. L. C. Jansen, A. A. Bakulin, *J. Am. Chem. Soc.* **2017**, *139*, 4068.
 [13] N. Onoda-Yamamuro, T. Matsuo, H. Suga, *J. Phys. Chem. Solids* **1992**, *53*, 935.
 [14] A. Glazer, *Acta Crystallogr. B* **1972**, *28*, 3384.
 [15] K. Miyata, L. Atallah Timothy, X. Y. Zhu, *Sci. Adv.* **2017**, *3*, e1701469.
 [16] Y. Guo, O. Yaffe, D. W. Paley, A. N. Beecher, T. D. Hull, G. Szpak, J. S. Owen, L. E. Brus, M. A. Pimenta, *Phys. Rev. Mater.* **2017**, *1*, 042401.
 [17] W.-J. Yin, J.-H. Yang, J. Kang, Y. Yan, S.-H. Wei, *J. Mater. Chem. A* **2015**, *3*, 8926.
 [18] P. S. Whitfield, N. Herron, W. E. Guise, K. Page, Y. Q. Cheng, I. Milas, M. K. Crawford, *Sci. Rep.* **2016**, *6*, 35685.
 [19] K. J. Lee, B. Turedi, A. Giugni, M. N. Lintangpradipto, A. A. Zhumekenov, A. Y. Alsalloum, J.-H. Min, I. Dursun, R. Naphade, S. Mitra, I. S. Roqan, B. S. Ooi, O. F. Mohammed, E. D. Fabrizio, N. Cho, O. M. Bakr, *Adv. Funct. Mater.* **2021**, *31*, 2008088.
 [20] N. Onoda-Yamamuro, T. Matsuo, H. Suga, *J. Phys. Chem. Solids* **1990**, *51*, 1383.
 [21] G. M. Bernard, R. E. Wasylshen, C. I. Ratcliffe, V. Terskikh, Q. Wu, J. M. Buriak, T. Hauger, *J. Phys. Chem. A* **2018**, *122*, 1560.
 [22] C. A. López, M. V. Martínez-Huerta, M. C. Alvarez-Galván, P. Kayser, P. Gant, A. Castellanos-Gomez, M. T. Fernández-Díaz, F. Fauth, J. A. Alonso, *Inorg. Chem.* **2017**, *56*, 14214.
 [23] T. Leijtens, G. E. Eperon, N. K. Noel, S. N. Habisreutinger, A. Petrozza, H. J. Snaith, *Adv. Energy Mater.* **2015**, *5*, 1500963.
 [24] C.-H. Lin, L. Hu, X. Guan, J. Kim, C.-Y. Huang, J.-K. Huang, S. Singh, T. Wu, *Adv. Mater.* **2022**, 2108616, <https://doi.org/10.1002/adma.202108616>.
 [25] L. McGovern, M. H. Futscher, L. A. Muscarella, B. Ehrler, *J. Phys. Chem. Lett.* **2020**, *11*, 7127.
 [26] G. Mannino, I. Deretzis, E. Smecca, A. La Magna, A. Alberti, D. Ceratti, D. Cahen, *J. Phys. Chem. Lett.* **2020**, *11*, 2490.
 [27] Z. Zhao, F. Gu, H. Rao, S. Ye, Z. Liu, Z. Bian, C. Huang, *Adv. Energy Mater.* **2019**, *9*, 1802671.
 [28] H. Gao, J. Feng, Y. Pi, Z. Zhou, B. Zhang, Y. Wu, X. Wang, X. Jiang, L. Jiang, *Adv. Funct. Mater.* **2018**, *28*, 1804349.
 [29] L. Chen, Y.-Y. Tan, Z.-X. Chen, T. Wang, S. Hu, Z.-A. Nan, L.-Q. Xie, Y. Hui, J.-X. Huang, C. Zhan, S.-H. Wang, J.-Z. Zhou, J.-W. Yan, B.-W. Mao, Z.-Q. Tian, *J. Am. Chem. Soc.* **2019**, *141*, 1665.
 [30] C. Quarti, E. Mosconi, J. M. Ball, V. D’Innocenzo, C. Tao, S. Pathak, H. J. Snaith, A. Petrozza, F. De Angelis, *Energy Environ. Sci.* **2016**, *9*, 155.
 [31] M. I. Saidaminov, A. L. Abdelhady, B. Murali, E. Alarousu, V. M. Burlakov, W. Peng, I. Dursun, L. Wang, Y. He, G. Maculan, A. Goriely, T. Wu, O. F. Mohammed, O. M. Bakr, *Nat. Commun.* **2015**, *6*, 7586.

- [32] W. Wang, J. Su, L. Zhang, Y. Lei, D. Wang, D. Lu, Y. Bai, *CrystEngComm* **2018**, *20*, 1635.
- [33] J. H. Noh, S. H. Im, J. H. Heo, T. N. Mandal, S. I. Seok, *Nano Lett.* **2013**, *13*, 1764.
- [34] S. A. Kulkarni, T. Baikie, P. P. Boix, N. Yantara, N. Mathews, S. Mhaisalkar, *J. Mater. Chem. A* **2014**, *2*, 9221.
- [35] Y. H. Park, I. Jeong, S. Bae, H. J. Son, P. Lee, J. Lee, C.-H. Lee, M. J. Ko, *Adv. Funct. Mater.* **2017**, *27*, 1605988.
- [36] S. Chai, X. Xiong, Y. Zheng, R. Shi, J. Xu, *Dalton Trans.* **2020**, *49*, 2218.
- [37] Z. Chen, Z. Luo, C. Huang, Y. Qi, P. Yang, L. You, C. Hu, T. Wu, J. Wang, C. Gao, T. Sritharan, L. Chen, *Adv. Funct. Mater.* **2011**, *21*, 133.
- [38] I. Anusca, S. Balčiūnas, P. Gemeiner, Š. Svirskas, M. Sanlialp, G. Lackner, C. Fettkenhauer, J. Belovickis, V. Samulionis, M. Ivanov, B. Dkhil, J. Banys, V. V. Shvartsman, D. C. Lupascu, *Adv. Energy Mater.* **2017**, *7*, 1700600.
- [39] S. Govinda, B. P. Kore, D. Swain, A. Hossain, C. De, T. N. Guru Row, D. D. Sarma, *J. Phys. Chem. C* **2018**, *122*, 13758.
- [40] D. H. Fabini, T. Hogan, H. A. Evans, C. C. Stoumpos, M. G. Kanatzidis, R. Seshadri, *J. Phys. Chem. Lett.* **2016**, *7*, 376.
- [41] M. Simenas, S. Balciunas, J. N. Wilson, S. Svirskas, M. Kinka, A. Garbaras, V. Kalendra, A. Gagor, D. Szewczyk, A. Sieradzki, M. Maczka, V. Samulionis, A. Walsh, R. Grigalaitis, J. Banys, *Nat. Commun.* **2020**, *11*, 5103.
- [42] B. Yang, W. Ming, M.-H. Du, J. K. Keum, A. A. Puzetzy, C. M. Rouleau, J. Huang, D. B. Geohegan, X. Wang, K. Xiao, *Adv. Mater.* **2018**, *30*, 1705801.
- [43] M. I. Dar, G. Jacopin, S. Meloni, A. Mattoni, N. Arora, A. Boziki, S. M. Zakeeruddin, U. Rothlisberger, M. Grätzel, *Sci. Adv.* **2016**, *2*, e1601156.
- [44] W. Kong, Z. Ye, Z. Qi, B. Zhang, M. Wang, A. Rahimi-Iman, H. Wu, *Phys. Chem. Chem. Phys.* **2015**, *17*, 16405.
- [45] C. Wehrenfennig, M. Liu, H. J. Snaith, M. B. Johnston, L. M. Herz, *APL Mater.* **2014**, *2*, 081513.
- [46] H.-H. Fang, R. Raissa, M. Abdu-Aguye, S. Adjokatse, G. R. Blake, J. Even, M. A. Loi, *Adv. Funct. Mater.* **2015**, *25*, 2378.
- [47] S. Tombe, G. Adam, H. Heilbrunner, D. H. Apaydin, C. Ulbricht, N. S. Sariciftci, C. J. Arendse, E. Iwuoha, M. C. Scharber, *J. Mater. Chem. C* **2017**, *5*, 1714.
- [48] C. Greenland, A. Shnier, S. K. Rajendran, J. A. Smith, O. S. Game, D. Wamwangi, G. A. Turnbull, I. D. W. Samuel, D. G. Billing, D. G. Lidzey, *Adv. Energy Mater.* **2020**, *10*, 1901350.
- [49] H. Z. Cummins, A. D. Buckingham, G. W. Series, E. R. Pike, J. G. Powles, *Philos. Trans. R. Soc. A* **1979**, *293*, 393.
- [50] A. Létoublon, S. Paofai, B. Rufflé, P. Bourges, B. Hehlen, T. Michel, C. Ecolivet, O. Durand, S. Cordier, C. Katan, J. Even, *J. Phys. Chem. Lett.* **2016**, *7*, 3776.
- [51] T. Chen, B. J. Foley, B. Ipek, M. Tyagi, J. R. D. Copley, C. M. Brown, J. J. Choi, S.-H. Lee, *Phys. Chem. Chem. Phys.* **2015**, *17*, 31278.
- [52] E. M. Mozur, J. R. Neilson, *Annu. Rev. Mater. Res.* **2021**, *51*, 269.
- [53] M. T. Dove, *Am. Mineral.* **1997**, *82*, 213.
- [54] A. C. Ferreira, S. Paofai, A. Létoublon, J. Ollivier, S. Raymond, B. Hehlen, B. Rufflé, S. Cordier, C. Katan, J. Even, P. Bourges, *Commun. Phys.* **2020**, *3*, 48.
- [55] D. Zhang, X. Hu, T. Chen, D. L. Abernathy, R. Kajimoto, M. Nakamura, M. Kofu, B. J. Foley, M. Yoon, J. J. Choi, S.-H. Lee, *Phys. Rev. B* **2020**, *102*, 224310.
- [56] F. Cordero, F. Craciun, F. Trequattrini, P. Imperatori, A. M. Paoletti, G. Pennesi, *J. Phys. Chem. Lett.* **2018**, *9*, 4401.
- [57] D. Yu, R. Mole, T. Noakes, S. Kennedy, R. Robinson, *J. Phys. Soc. Jpn.* **2013**, *82*, 034718.
- [58] D. Yu, R. A. Mole, G. J. Kearley, *Performance Test on PELICAN – A Multi-Purpose Time of Flight Cold Neutron Spectrometer*, EDP Sciences, France **2015**.
- [59] J. P. Perdew, A. Ruzsinszky, G. I. Csonka, O. A. Vydrov, G. E. Scuseria, L. A. Constantin, X. Zhou, K. Burke, *Phys. Rev. Lett.* **2008**, *100*, 136406.
- [60] G. Kresse, J. Furthmüller, *Phys. Rev. B* **1996**, *54*, 11169.
- [61] A. K. Sagotra, D. Chu, C. Cazorla, *Phys. Rev. Mater.* **2019**, *3*, 035405.